20 GHz Antenna Radiation Pattern Obtained From Near-Field Mapping With Electrooptic Probe on a Single Plane

Gwenael Gaborit, Philippe Artillan, Cédric Bermond, Guillaume Revillod, Guillaume Chevrier-Gros, Lionel Duvillaret

20 GHz antenna radiation pattern obtained from near field mapping with electro-optic probe on a single plane

G. Gaborit, P. Artillan, C. Bermond, G. Revillod, G. Chevrier-Gros and L. Duvillaret

***Abstract*—The ability of an electro-optic sensor to perform near-field mapping of a 20 GHz pyramidal horn antenna without disturbance on the radiation behavior is demonstrated. The electric field is scanned on a plane close to the horn aperture with spatial resolution less than $0.1\lambda_0$. The dynamic range reaches more than 40 dB. The measured magnitudes and phases of near field pixels enable the computation of the far-field radiation pattern. The results are in excellent agreement with theory, numerical simulations and actual far-field measurement. The different approaches lead to the same antenna gain with a confidence interval lower than 1 dB. Furthermore, the behaviour of the electromagnetic wave from reactive to radiative region is investigated. The weak invasivenes of the probe is also analysed.**

***Index Terms*—Antenna radiation pattern, electro-optic sensor, electric field mapping, Ka-band, near field sensing.**

I. Introduction

CHACTERIZATIONS of the radiation pattern of microwave antennas have historically been performed in far field. Thus, the measurement set-up requires an anechoic chamber of appropriate size. Moreover, the sensors mainly used for this analysis are metallic antennas. The distance between the antenna under test (AUT) and the measuring antenna have then to be large enough to avoid electromagnetic (EM) coupling. Other techniques such as bolometer or calorimeter can also be used, but they only provide quadratic responses with no phase information [1]–[8]. Infrared thermography of an RF sensitive film is another alternative that directly leads to the transverse field distribution [9]–[18]. Some efficient commercial solutions are also available [19], [20]. Based on an array of dual antennas, they offer fast and valuable antenna characterization, but still in the far-field region. Nevertheless, electro-optic (EO) technique provide many advantages for E-field analysis [21]–[34]. The intrinsic dynamic range of EO sensors exceeds 120 dB, from less than 1 V/m up to more than 1 MV/m. A single probe covers more than 9 decades of frequency and can even reach the THz band in equivalent time domain [35]. The measurement voxel of such a probe is less than 1 mm^3, *i.e.* $\frac{\lambda}{15}$ at 20 GHz for one dimension. Finally, EO probes are millimetre size and their structure is fully dielectric, thus minimizing the disturbance of the AUT. Using an optical fiber, they authorize remote measurements up to more than 100 meters without dispersion. We here give a comprehensive analysis of a directive horn antenna with a special emphasis on the weak disturbance induced by the EO probe. After describing the measurement setup and especially the developped EO probe in Section II, the experimental results of transverse and longitudinal mappings of E-field in the vicinity of the antenna are presented in Section III. Finally, the calculated far-field radiation pattern of the antenna are given and compared to theoretical values in section IV.

Paper submitted in April 2020

P. Artillan, C. Bermond and G. Gaborit are with Univ. Grenoble Alpes, Univ. Savoie Mont Blanc, CNRS, Grenoble INP, IMEP-LAHC, 38000 Grenoble, France (e-mail: gwenael.gaborit@univ-smb.fr).

G. Revillod, G. Chevrier-Gros, L. Duvillaret and G. Gaborit are with Kapteos S.A.S., Bât Cleanspace, 354 Voie Magellan, 73800 Sainte-Hélène-du-Lac, France (e-mail: lionel.duvillaret@kapteos.com).

The authors would like to acknowledge the DGA (French Military Programs Management and Procurement Agency) for financial support in the SOLSTICE project.

II. Measurement set-up

The vector E-field sensor is an EO probe developed by Kapteos. The probe is based on an EO crystal (BSO crystal). This EO crystal acts as a polarization state modulator (PSM) for a laser probe beam crossing forth and back the crystal placed in front of the AUT. This PSM is then converted into a modulation of the optical intensity. Depending on the crystal cut, this PSM is induced either by the E-field component longitudinal to the sensor or transverse to it [32]. The transducer is mechanically protected by a multilayer dielectric sheath which also provides an impedance matching between the air and the crystal, in terms of permittivity. A detailled description and performances of the probe can be found elsewhere [36]–[39]. A high speed photo-receiver, embedding a low noise amplifier, finally delivers an electrical signal proportional to the E-field component to be measured. The electrical signal is then amplified thanks to a low noise amplifier. The whole set-up is described in Fig.1.

Since both the optoelectronic unit and the EO probe are temperature dependent free, the full experiment can be set up in any room without requiring air conditioning. The AUT is a pyramidal horn antenna Narda WR51 with a typical gain of 20 dBi. Its transverse dimensions are 64 mm×49 mm. The measurements have been performed with a Vector Network Analyser (VNA) Anritsu 37397C (40 MHz - 65 GHz). A preliminary one-port measurement of the antenna with and without the EO probe has demonstrated the very weak disturbance induced the probe (cf. Fig.2). In the frequency range from 19.8 GHz to 20.2 GHz, The S_{11} magnitude remains below -25 dB, even in the presence of the probe. A nominal frequency of 20 GHz is then chosen for further measurements.

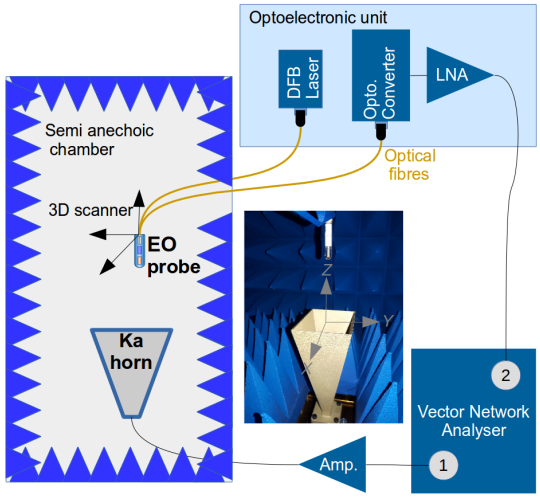

Fig. 1. Experimental set-up dedicated to the near electric field mapping of a horn antenna. A photography of the EO probe in front of the antenna is given in the center of the figure. (DFB laser stands for distributed feedback laser diode).

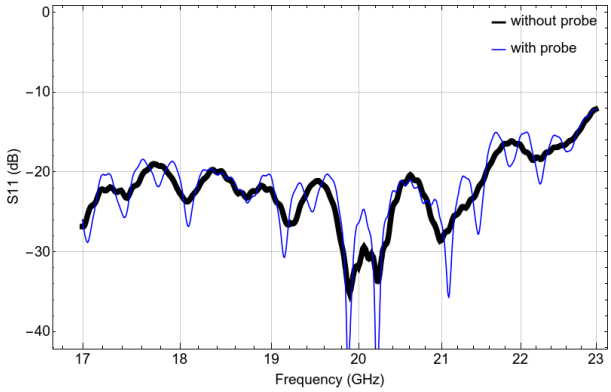

Fig. 2. Reflection coefficient of the antenna. Black curve: S_{11} of the antenna without the EO probe (reference). Blue curve: S_{11} of the antenna with EO probe placed in the reactive region (within the horn, in the vicinity of the apex).

In the setup presented in Fig. 1, the VNA is only used as a one-way bridge to measure the transmission scaterring parameter S_{21}. The measured S_{21} parameter is a linear image of the E-field vector component adressed by the probe. VNA port 1 is set at the maximum output power (-7 dBm) and connected to a 30 dB power amplifier to feed the AUT. VNA port 2 is used to receive the transduced EO signal delivered by the output of the optoelectronic unit. A preliminary SOLT calibration places the reference planes at the outputs of the power amplifier and the EO optoelectronic unit. The calibration is mostly performed to eliminate the unknown switch terms, whereas uncalibrated measurements would otherwise give good results. The intermediate frequency bandwidth is set to 10 Hz for all measurements in order to achieve the maximum sensitivity but a higher value could have been chosen to fasten the measurement time with still acceptable dynamic range. The EO probe is mounted on a 3D printed dielectric and faceted support thus avoiding parasitic reflections. The support is moved by a Cartesian robot synchronised with the VNA acquisition.

III. Near field experimental results

A. Transverse mapping of the E-field

The relative magnitude and the relative phase of the E-field radiated by the AUT have first been measured at 5 mm from its aperture. The scanning step was 2 mm, which is greater than the transverse spatial resolution of the probe (≈ 500 μm) and much smaller than the wavelength at 20 GHz ($\lambda = 15$ mm). With this 2 mm$\times$2 mm spatial step in both direction X and Y, the E-field mapping is composed of 1575 pixels. The raw measurements are shown on Fig. 3.a/b at 20 GHz and Fig. 3.c/d at 19.52 GHz. As can be seen on Fig. 3.a, the near-field measurement dynamics exceeds 40 dB. A comparison between the two close frequency points shows the extreme variability of the near-field behaviour of the antenna. The theoretical data corresponding to those measurements have been simulated with HFSS full wave solver of Ansys Electronics Desktop and are presented in Fig. 3.e/f. Due to small differences between the theoretical and the actual physical geometry of the antenna, the 20 GHz simulation corresponds, in fact, to the 19.52 GHz measurement. A second transverse plane at 120 mm from the aperture of the antenna has been scanned experimentally and simulated (cf. Fig. 4). The very good agreement between measurement and simulation validates the EO measurement approach.

B. Longitudinal mapping of the E-field

The Cartesian robot has also been used to provide the vector E-field in the E-plane and H-plane and the results are presented and compared to simulations in Fig. 5. It is important to note that the signal to noise ratio remains greater than 40 dB for both mappings, even if the dynamic range of the E-plane mapping is smaller due to much higher homogeneity of the field over the scanned surface.

Fig. 6 presents the phase of the E-field along Z-axis for $X = Y = 0$ (probe in the symmetry axis of the horn antenna). The unwrapped measured phase is very close to the theoretical phase, *.i.e.* the phase corresponding to propagation at light speed. As noticed on the inset of Fig. 6, the relative error is less than 0.5 % for $Z \geq 20$ mm. It is due to the 20 μm Cartesian robot positioning accuracy. For positions of the probe in the very vicinity of the antenna, the relative error on the phase increases due to a measurement artefact: the effective dielectric permittivity of the probe ($\epsilon r_{eff} \approx 3.6$) slightly influences the effective permittivity viewed by the propagating wave, thus sightly reducing the wave velocity. This result gives a practical method to determine the minimum acceptable distance for near-field measurements.

IV. Near-field to far-field transformation and results

A. Radiation pattern

In order to extract the far field pattern, each pixel of the mapping is firstly considered as a punctual and spherical electromagnetic wave source. Using classical diffraction theory,

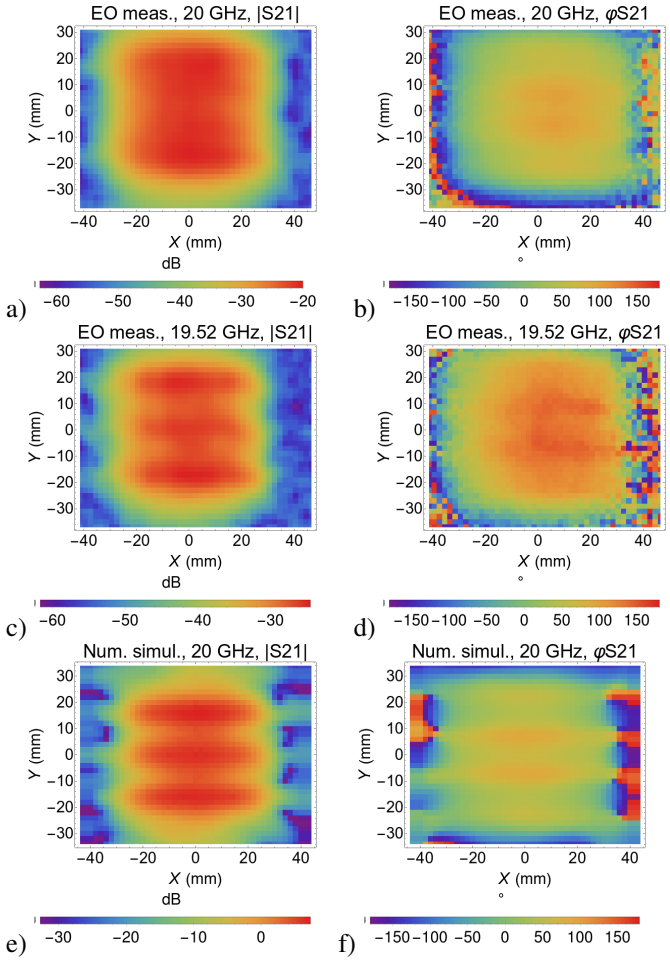

Fig. 3. Measured and simulated 2D transversal mapping of the E-field at 5 mm from the aperture of the antenna.

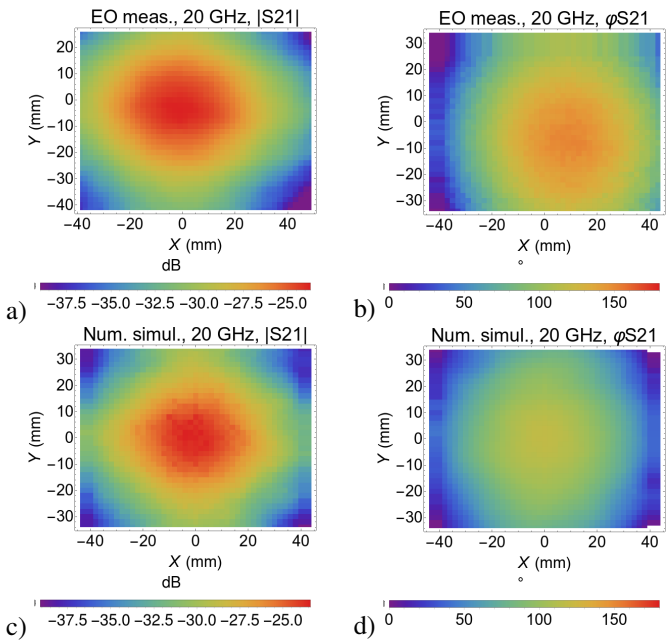

Fig. 4. Measured and simulated 2D transversal mapping of the E-field at 120 mm from the aperture of the antenna.

one can calculate the radiated field at a position (X,Y,Z)

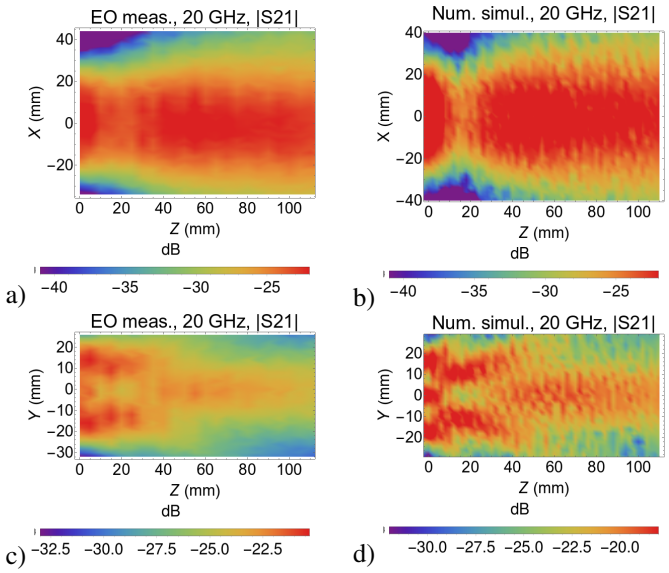

Fig. 5. Measured and simulated 2D longitudinal mapping of the E-field magnitude starting at the aperture of the antenna.

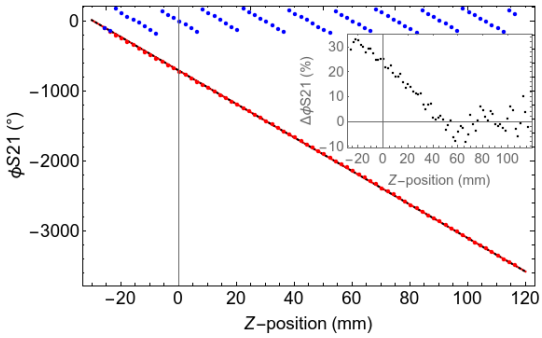

Fig. 6. Phase of the E-field as a function of the distance to the antenna ($Z = 0$ corresponds to the aperture plane). Blue and red dots correspond to the raw data and to the unwrapped phase, respectively. The red line is a linear fitting curve. Dashed black line is the theoretical line. The inset indicates the relative error between measurement and fit as a function of the distance.

located in the Fraunhofer region. The used near-field to far-field transformation equation is given below:

$$E(X,Y,Z) \propto \sum_i \frac{|E_i|}{r} e^{j(\varphi_i + \frac{2\pi f}{c} r)} K(\theta) \qquad (1)$$

$|E_i|$ and φ_i are the modulus and the phase of the *ith*-pixel. r is the euclidian distance between the considered pixel and the point (X,Y,Z). $K(\theta)$ is an obliquity factor which is equal to $\frac{\cos\theta+1}{2}$ in the Kirchhoff formulation and equal to 1 in the Rayleigh-Sommerfeld formulation. The use of eq. 1 leads to the experimental radiation pattern presented on Fig. 7 (blue curve). The near-field to far-field computation method proposed in this paper is based on a well-established algorithm using plane wave spectrum (PWS) [40], [41]. A known limitation to this method is that the field is assumed to vanish outside of the measurement window. However, this simple method proves to be very efficient for the horn antenna case with a correctly sized window and the obtained results give a fully satisfying proof of concept for electro-optic near-field measurement aiming at the computation of

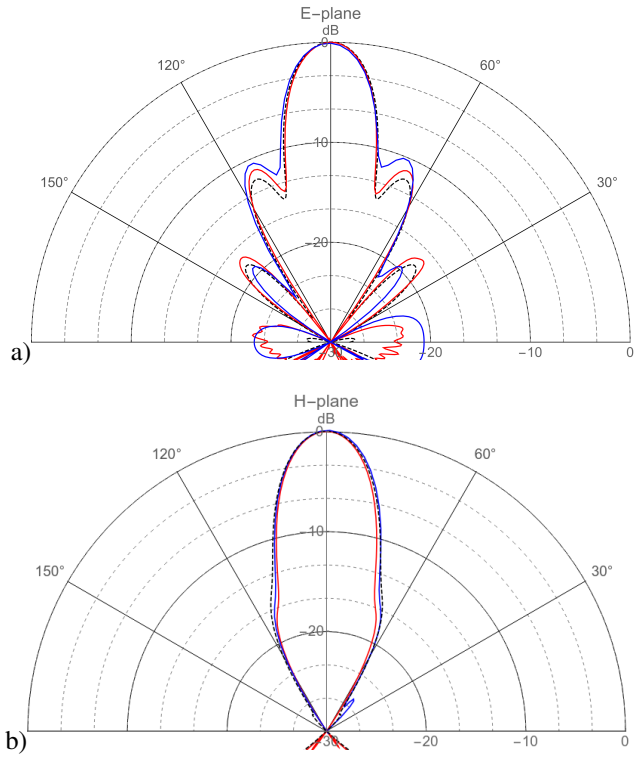

Fig. 7. Radiation patterns of the antenna at the operating frequency (20 GHz). The blue line is calculated from the near field mapping. The red line corresponds to numerical simulations (ANSYS HFSS). The black dashed line is the theoretical radiation patterns obtained thanks to equations 2 and 3. a) Angular distribution of the field in the E-plane. b) Angular distribution of the field in the H-plane

a radiation pattern. Further developments are to be tested to avoid the measurement window limitation, the planar regular rectangular grid and to fasten the computation time, thus enabling real-time visualization. This could be achieved by using approximated equivalent current method algorithms such as proposed in ref. [42], [43]. The theoretical radiation pattern of the measured pyramidal horn antenna can be obtained by its closed-form expression [44]–[46] (black dashed curves) or by simulation (red curves). Both are in very good agreement with the experimental radiation pattern. For the sake of completeness, the theoretical expression of the radiation pattern in E-plane and H-plane are given here, coming from Huygens-Fresnel principle:

$$E_{E-plane}(\theta) = (1+\cos\theta)\int_{-a/2}^{a/2} e^{j\frac{2\pi f}{c}(x\sin\theta-\frac{x^2}{2\rho_E})}dx \quad (2)$$

$$E_{H-plane}(\theta) = (1+\cos\theta)\int_{-b/2}^{b/2} \cos(\frac{\pi y}{b})e^{j\frac{2\pi f}{c}(y\sin\theta-\frac{y^2}{2\rho_H})}dy \quad (3)$$

where a and b are the transverse dimensions of the aperture of the antenna and ρ_E (*resp.* ρ_H) is the distance between the E-plane (*resp.* H-plane) apex and the aperture of the pyramidal horn antenna.

TABLE I
GAIN OF THE ANTENNA AT 20 GHZ

Source	$\theta_{E-plane}$ (°)	$\theta_{H-plane}$ (°)	Gain G (dBi)
Manufacturer data	16.9	18	21.3
Mapping at 120 mm	16.3	17.7	21.5
Mapping at 5 mm (eq.1)(1)	15.3	16.3	22.2
Mapping at 5 mm (eq.1)(2)	15.6	16.6	22
Numerical simulations	15.2	16.1	22.2
Theory (eq.2 and eq.3)	15.7	16.7	21.9

(1) and (2), correspond to $K(\theta) = 1$ and $K(\theta) = \frac{\cos\theta+1}{2}$, respectively.

B. Half power beam width and gain

The extraction of the radiation pattern of the antenna at 20 GHz allows the evaluation of the half power beam width (HPBW) both in E-plane and H-plane (θ_E and θ_H). The gain G of the antenna is then obtained thanks to the empirical equation 4.

$$G = 10\log_{10}(\frac{41000}{\theta_E\theta_H}), \quad (4)$$

Table I summarizes the various values of θ_E, θ_H and G obtained from near-field mappings at various distances and using various obliquity factor formulas. The mapping realized at 120 mm gives results very close to the constructor data. As explained in part III-B, at that distance, the disturbance induced by the dielectric probe is negligible. This result demonstrates both the quality of the near-field measurement and the applicability of eq. 1. The other computations are also very close one from each other, thus validating the possiblity to make very close measurements from the antenna. Finally, the slight variation between the two theoretical approaches using two different obliquity factor expressions can be explained by the small phase variation of the E-field phase at the vicinity of the aperture of the pyramidal horn. For other types of antennas, a careful study of the impact of this factor would be of key importance. Last point of the discussion concerns the resolution of the near field mapping: degraded images with a spatial resolution of $\lambda/3$ would have lead to an error on the gain extraction of less than 1 dBi. This is due to the quite homogeneous field distribution in the vicinity of the AUT.

V. CONCLUSION

A non invasive electro-optic probe dedicated to the near-field scanning of an antenna has been demonstrated with at least 40 dB dynamic range. Its use with a VNA enables high resolution mapping of the field in the reactive near field region of the antenna. The extraction of the far-field parameters (radiation pattern, antenna gain and half power beam width) of the antenna has been demonstrated and a methodology has been proposed. The results in terms of radiation pattern, gain and half power beam width are in good agreement with theory, simulations and constructor data. Further investigations will include the measurement of various types of antennas for 5G applications and aerospatial, including arrays of antenna and antenna embedded with application-specific integrated circuits.

REFERENCES

[1] M. Galeazzi and D. McGammon, "Microcalorimeter and bolometer model," *J. Appl. Phys.* **93**, pp. 4856–4869, 2003.

[2] P. D. Mauskopf, J. J. Bock, H. D. Castillo, W. L. Holzapfel, and A. E. Lange, "Composite infrared bolometers with Si_3N_4 micromesh absorbers," *Appl. Opt.* **36**, pp. 765–771, 1997.

[3] J. M. Gildemeister, A. T. Lee and P. L. Richards, "A fully lithographed voltage-biased superconducting spiderweb bolometer," *Appl. Phys. Lett.* **74**, pp. 868–870, 1999.

[4] S. A. Dayeh, D. P. Butler and Z. Çelik-Butler, "Micromachined infrared bolometers on flexible polyimide substrates," *Sensors Actuators A* **118**, pp. 49–56, 2005.

[5] J. Glenn, G. Chattopadhyay, S. Edgington, E. Lange, J. Bock, D. Mauskopf and T. Lee, "Numerical optimization of integrated cavities for diffraction-limited millimetre-wave bolometer arrays," *Appl. Opt.* **41**, pp. 136–142, 2002.

[6] V.Y. Zerov, Y.V. Kulikov, V.N. Leonov, V.G. Malyarov, I.A. Khrebtov and I.I.Shaganov, "Features of the operation of a bolometer based on a vanadium dioxide film in a temperature interval that includes a phase transition," *J. Opt. Technol.* **66**, pp. 387–390, 1999.

[7] C. Kittel, "Physique de l'état solide," 1983.

[8] L. Brunetti and E. T. Vremera, "A new microcalorimeter for measurements in 3.5-mm coaxial line," *IEEE Trans. Instrum. Meas.* **52**, pp. 320–323, 2003.

[9] C. Meola and G. M. Carlomagno, "Recent advances in the use of infrared thermography," *Meas. Sci. Technol.* **15**, pp. R27–R58, 2004.

[10] J. Norgard, J. Will, and C. Stubenrauch, "Quantitative images of antenna patterns using infrared thermography and microwave holography," *International J. Imaging Systems Technol.* **11**, p. 210, 2000.

[11] F. Tristant, J.-P. Moreau, and P. Levesque, "Electromagnetic measurement in a mode-stirred chamber," *Microwave Opt. Technol. Lett.* **28**, p. 417, 2001.

[12] P. Levesque and D.-L. Balageas, "Single-sided interferpmetric EMIR method for NDE of structures," *Quantitative Infrared Thermography, Lodz - Pologne* , 7 - 10 septembre 1998.

[13] D. W. Metzger, J. D. Norgard and R. M. Sega, "Near-field patterns from pyramidal horn antennas : numerical calculation and experimental verification," *IEEE Trans. Electromagn. Compat.* **33**, pp. 188–196, 1991.

[14] P. Levesque, L. Leylekian and D. Balageas, "Vectorial characterisation of electromagnetics fields by infrared thermography," *Quantitative Infrared Thermography, Remis - France*, 2000.

[15] J. D. Norgard, R. M. Sega, M. G. Harrison and H. H. Pohle, "Infrared mapping of transient electromagnetic fields radiated by high power microwave pulsed sources," *IEEE Trans. Nuclear Sci.* **39**, pp. 1912–1920, 1992.

[16] B. Pliquet, P. Levesque, B. Duchêne, X. Ferrieres and J.-C. Alliot , "Electromagnetic nondestructive evaluation of materials from incomplete EMIR data," *Annual Review of Progress in Quantitative Nondestructive Evaluation, Montréal - Canada*, 1999.

[17] R. W. Astheimer and F. Schwarz, "Thermal imaging using pyroelectric detectors," *Appl. Opt.* **7**, pp. 1687–1695, 1968.

[18] S. Huth, O. Breitenstein, A. Hauber, D. Dantz, U. Lambert and F. Altmann, "Lock-in IR-thermography - A novel tool for material and device characterization," *Solid State Phenomena* **82-84**, p. 741, 2002.

[19] https://www.mvg-world.com/fr/satimo-is-mvg

[20] http://www.ets-lindgren.com/solutions/antenna-pattern-measurements

[21] K. Yang, G. David, J.-G. Yook, I. Papapolymerou, L. P. B. Katehi and J. F.Whitaker, "Electrooptic mapping and finite-element modeling of the near-field pattern of a microstrip patch antenna," *IEEE Trans. Microwave Theory Tech.* **48**, pp. 288–294, 2000.

[22] A. Yariv, "Optical Electronics," 1991.

[23] L. Duvillaret, S. Rialland and J. L. Coutaz, "Electro-optic sensors for electric field measurements. I. Theoretical comparison among different modulation techniques.," *J. Opt. Soc. Am. B* **19**, pp. 2692–2703, 2002.

[24] M.-S. Huang, M.-H. Lu and J.-T. Shy, "High sensitivity bulk electro-optic modulator field sensor for high voltage environments," *Rev. Sci. Instrum.* **75**, pp. 5364–5366, 2004.

[25] K. Tajima, R. Kobayashi and N. Kuwabara, "Experimental evaluation of broadband isotropic electric field sensor using three Mach-Zehnder interferometers," *Electron. Lett.* **34**, pp. 1130–1132, 1998.

[26] W. K. Kuo, S. -L. Huang, T. S. Horng and L. C. Chang, "Two-dimensional mapping of the electric-field vector by electro-optic prober," *Opt. Comm.* **149**, pp. 55–60, 1998.

[27] W. K. Kuo, Y. -T. Huang and S.-L. Huang, "Three-dimensional electric-field vector measurement with an electro-optic sensing technique," *Opt. Lett.* **24**, pp. 1546–1548, 1999.

[28] W. K. Kuo, W.-H. Chen, Y.-T. Huang and S.-L. Huang, "Two-dimensional electric-field vector measurement by a $LiTaO_3$ electro-optic tip," *Appl. Opt.* **39**, pp. 4985–4993, 2000.

[29] K. J. Weingarten, M. J. W. Rodwell and D. M. Bloom, "Picosecond optical sampling of GaAs integrated circuits," *IEEE J. Quantum Electron.* **24**, pp. 198–220, 1988.

[30] R. Kobayashi, K. Tajima, N. Kuwabara and M. Tokuda, "Improvement of frequency characteristics of electric field sensor using mach-Zehnder interferometer," *Electron. Comm. Jpn Pt* **83**, pp. 76–84, 2000.

[31] D. H. Naghski, J. T. Boyd, H. E. Jackson, S. Sriram, S. A. Kingsley and J.Latess, "An integrated photonic Mach-Zehnder interferometer with no electrodes for sensing electric fields," *J. Lightwave Technol.* **12**, pp. 1092–1097, 1994.

[32] L. Duvillaret, S. Rialland and J.L. Coutaz, "Electro-optic sensors for electric field measurements. II. Choice of the crystals and complete optimization of their orientation," *J. Opt. Soc. Am. B* **19**, pp. 2704–2715, 2002.

[33] K. Sabet, R. Darragh, A. Sabet, K. Sarabandi, and L. P. Katehi, "Using electro-optic field mapping for design of dual-band circularly polarized active phased arrays," *IEEE 18th Wireless and Microwave Technology Conference (WAMICON)* pp. 1–5, 2017.

[34] K. Sarabandi, J. Choi, A. Sabet, and K. Sabet. (2016). "Pattern and gain characterization using nonintrusive very-near-field electro-optical measurements over arbitrary closed surfaces," *IEEE Transactions on Antennas and Propagation*, **65**, 2, pp. 489–497, 2017.

[35] F. Sanjuan, G. Gaborit and J.-L Coutaz, "Full electro-optic terahertz time-domain spectrometer for polarimetric studies", *App. Opt.*, **57**, 21, pp. 6055-6060, 2018.

[36] G. Gaborit, J.-L. Coutaz and L. Duvillaret, "Vectorial electric field measurement using isotropic electro-optic crystals",*Appl. Phys. Lett.*, **90**, 241118, 2007.

[37] M. Bernier, L. Duvillaret, G. Gaborit, A. Pauper and J.-L. Lasserre, "Fully-automated E-field measurement system using pigtailed electro-optic sensors for temperature-dependent-free measurements of microwave signals in outdoors conditions", *IEEE Sens. J.*, **9**, No. 1, pp. 61-68, 2009.

[38] G. Gaborit, J. Dahdah, F. Lecoche, P. Jarrige, Y. Gaeremynck, E. Duraz, and L. Duvillaret, "A Nonperturbative Electrooptic Sensor for in Situ Electric Discharge Characterization", *IEEE Trans. Plasma Sci.*, **41**, 10, pp. 2851-2857, 2013.

[39] G. Gaborit, P. Jarrige, F. Lecoche, J. Dahdah, E. Duraz, C. Volat and L. Duvillaret, "Single Shot and Vectorial Characterization of Intense Electric Field in Various Environments with Pigtailed Electro-optic Probe", *IEEE Trans. Plasma Sci.*, **42**, 5, pp. 1265-1273, 2014.

[40] R.C. Johnson, H.A. Ecker and J.S. Hollis, "Determination of far-field antenna patterns from near-field measurements", *Proc. IEEE*, **61**, 12, pp. 16681694, 1973.

[41] C.H Schmidt and T.F. Eibert, "Near-field to far-field transformation utilizing multilevel plane wave representation for planar and quasi-planar measurement contours", *IET Microw. Antennas Propag.*, **4**, 11, pp. 18291837, 2010.

[42] R. R. Alavi, A. Kiaee, R. Mirzavand, and P. Mousavi. "RWG MoM-via-locally corrected Nystrm method in near-field to far-field transformation using very-near-field measurement", *IET Microwaves, Antennas and Propagation*, **12**, 2, pp. 145-153, 2017.

[43] A. Kiaee, R. R. Alavi, R. Mirzavand, and P. Mousavi. "Numerical and Experimental Assessment of Source Reconstruction for Very Near-Field Measurements With an Array of H-Field Probes", *IEEE Transactions on Antennas and Propagation*, **66**, 3, pp. 1311-1320, 2017.

[44] C. A. Balanis, "Antenna theory: Analysis and design," New York, Harper and Row, Publishers, 1982.

[45] S. A. Schelkunoff and H. T. Friis, "Antennas: theory and practice," New York: Wiley, 1952.

[46] M. J. Maybell and P. S. Simon, "Pyramidal horn gain calculation with improved accuracy," *IEEE transaction on antenna and propropagation*, **41**, no. 7, pp. 884–889, 1993.